High-temperature high-pressure phases of lithium from electron force field (eFF) quantum electron dynamics simulations

Hyungjun Kim[a], Julius T. Su[b], and William A. Goddard III[a,b,1]

[a]Center for Materials Simulations and Design, Graduate School of Energy, Environment, Water, and Sustainability (World Class University), Korea Advanced Institute of Science and Technology, Daejeon 305-701, Republic of Korea; and [b]Materials and Process Simulation Center, California Institute of Technology, Pasadena, CA 91125

Contributed by William A. Goddard III, July 11, 2011 (sent for review November 3, 2010)

We recently developed the electron force field (eFF) method for practical nonadiabatic electron dynamics simulations of materials under extreme conditions and showed that it gave an excellent description of the shock thermodynamics of hydrogen from molecules to atoms to plasma, as well as the electron dynamics of the Auger decay in diamondoids following core electron ionization. Here we apply eFF to the shock thermodynamics of lithium metal, where we find two distinct consecutive phase changes that manifest themselves as a kink in the shock Hugoniot, previously observed experimentally, but not explained. Analyzing the atomic distribution functions, we establish that the first phase transition corresponds to (*i*) an fcc-to-cI16 phase transition that was observed previously in diamond anvil cell experiments at low temperature and (*ii*) a second phase transition that corresponds to the formation of a new amorphous phase (amor) of lithium that is distinct from normal molten lithium. The amorphous phase has enhanced valence electron-nucleus interactions due to localization of electrons into interstitial locations, along with a random connectivity distribution function. This indicates that eFF can characterize and compute the relative stability of states of matter under extreme conditions (e.g., warm dense matter).

wavepacket dynamics | interstitial electron model | symmetry breaking

There are great uncertainties in the properties of matter at the high compression (several times ambient densities) and high temperatures (20,000–2,000,000 K) characteristic of deep interiors of giant planets (1), conditions of thermonuclear fusion, and phenomena generated by shocks from planetary impact (2). New methods for experimental study of these regimes are being developed (National Ignition Facility at Lawrence Livermore National Laboratory, Z-Pinch at Sandia National Laboratory) that generate data about materials under extreme conditions. However, theoretical and computational methods used to predict properties of warm dense matter [high temperatures (T), high pressures (P), and under rapidly changing conditions] have serious shortcomings leading to considerable uncertainties due to high degrees of electronic excitation, structural and electronic heterogeneity, and complex transient dynamics. This contrasts with the situation at room temperature (RT), where a wealth of structural and energetic data on compressed phases is available via experiments in diamond anvil cells and gas guns (3–5), and from theoretical studies such as density functional theory (DFT).

To provide fresh insight into the dynamical properties of warm dense matter, we developed the eFF (electron force field) methodology that explicitly solves the time-dependent Schrödinger equation including all two-body interactions, with the restrictions that the electrons are described as Gaussian wave packets and that the wavefunction is described as a Hartree product (with exchange terms replaced by a spin dependent Hamiltonian). The eFF makes it practical to describe the nonadiabatic quantum dynamics of extended systems containing highly excited electrons at a computational cost comparable to that of classical molecular dynamics (6). This allows the dynamics of electrons and nuclei to be treated on an equal footing, without the adiabatic assumption of first solving for stationary states of the electrons. This nonadiabatic approach is very important for the systems at high temperature range (>10,000 K) because the substantial kinetic energy of the electrons makes their dynamics no longer subordinate to the dynamics of nuclei. Thus the eFF method provides a useful complement to current DFT methods, which are based on ground state electronic theory, and hence may not properly handle electronic dynamics for rapidly evolving systems. It is also a complement to classical force field methods, which contain no explicit description of electron dynamics.

Previously, we reported the use of eFF to simulate the shock thermodynamics of hydrogen, including the transformation from molecules to atoms to plasma under high temperatures and compressions (see Figs. S1 and S2) (7). We also reported the application of eFF to describing the electron dynamics of the highly excited states in diamonoid nanoparticles formed by relaxation of valence electrons into core holes (Auger process) (8). These studies agree with available experimental data.

Here we extend the eFF into systems containing both tightly bound core electrons and loosely bound metallic electrons, where previous wave packet methods have had considerably difficultly. The alkali metals were long thought to be rather simple nearly free-electron metals, but in the last decade have been shown to be rather complex, with localization transitions at high P (9–17). The spherical shape of the ground state orbital led initially to the belief that the solid would not exhibit phase transitions beyond the highly coordinated phases; i.e., face-centered cubic (fcc) phase after body-centered cubic (bcc) under high pressure (Figs. S3–S5) (18). This description of alkali metals in terms of nuclear-centered s-like valence electrons was shown to be incorrect from generalized valence bond calculations on Li clusters (19) and later from DFT calculations on bulk Li (20), which predicted that Li would undergo a symmetry breaking solid-solid phase transition. The driving force for these structural distortions is the shifting of the valence electrons to interstitial positions between the nuclei, leading to strong bonds of a single electron to several nuclei. The increased stability of these interstitial-centered electrons provides the driving force toward decreased nuclear coordination number (CN) of the solid at high pressures.

Such predictions stimulated X-ray diffraction experiments of compressed Li (10), that found a transition from fcc (CN 12) to the cI16 (CN 11) structure in which each electron is close to eight nuclei. This was followed by further DFT studies showing the cI16 (9, 21–24) structure to be stable at high P and low T

Author contributions: H.K., J.T.S., and W.A.G. designed research; H.K. performed research; H.K., J.T.S., and W.A.G. analyzed data; and H.K., J.T.S., and W.A.G. wrote the paper.

The authors declare no conflict of interest.

[1]To whom correspondence should be addressed. E-mail: wag@wag.caltech.edu.

This article contains supporting information online at www.pnas.org/lookup/suppl/doi:10.1073/pnas.1110322108/-/DCSupplemental.

PHYSICS

(11, 25). However no attempts have been made to understand what happens at high pressures and temperatures.

Here we apply eFF to compute the electronic and structural properties of phases of lithium over a wide range of temperatures and pressures (up to 20,000 K and 100 GPa), with comparisons to experiments capable of accessing those extreme conditions.

Results and Discussion

To validate that eFF leads to a correct description of the fcc-to-cI16 transition under ambient conditions, we performed isothermal dynamics at 300 K on fcc and cI16 lattices at various densities [$\rho = 0.53$ (normal) to 1.5 g/cm^3]. We find that eFF describes both structures well, with predicted X-ray diffraction patterns exactly matching those from the experiment of (10) (see Fig. S6) including the transition at $P = 40$ GPa (see Fig. S7).

The locations and sizes of the valence electrons, as well as the positions of the nuclei, change over the course of eFF dynamics (see Fig. 1). For both the fcc and cI16 structures, eFF leads to valence electrons located in interstitial positions between several nuclei, in agreement with the interstitial electron (IE) model of Li (19, 26). For the metallic fcc phase, we find IEs located at octahedral interstices between Li^+ ions (six coordinate), whereas in the semimetallic cI16, half of the IEs are located inside trapezoidal zigzag chains in the (010) direction, with the other half sitting in between ions bridging the chains (eight coordinate but with four shorter bonds). These locations are identical to the electron density maxima observed in DFT calculations (10).

We then proceeded to compute the shock behavior of Li solid, assuming that a thermodynamic equilibrium is established in the bulk solid as the shock front passes through (27). Under those conditions, the pressure P, volume V, and internal energy E satisfy the Rankine–Hugoniot equation: $E\text{-}E_0 + (1/2)(V\text{-}V_0)(P + P_0) = 0$, where the subscript zero denotes the initial state before the compression (taken to be $\rho_0 = 0.53$ g/cm^3 and $T_0 = 291$ K). We performed eFF dynamics on systems of varying ρ and T to determine P, V, and E satisfying the above equation. The initial structure in each case was taken to be either fcc or cI16, depending on which structure had a lower internal energy at the given ρ. The detailed procedure is described in the method section.

Fig. 2 shows that the resulting eFF Hugoniot curve matches experiments (28–31), including a kink at 1.2 to 1.3 g/cm^3 and 50 GPa. To understand and characterize the microscopic origin of this effect, we show in Fig. 3*A* the nuclear pair distribution functions, g(r), for various points on the Hugoniot curve. Here, the axis is scaled by $r_s = (3/4\pi n)^{1/3}$, where n is the number density. Integrating g(r) until the first minimum leads to the CN for each atom (see Fig. S8*B*).

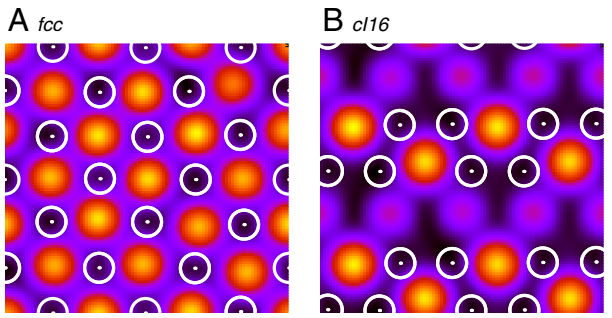

Fig. 1. The eFF finds as global minima valence electrons in Li that are centered at interstitial sites between Li^+ ions. (*A*) The eFF electron density map of valence electrons for fcc Li solid at ambient density ($\rho = 0.53$ g/cm^3). Shown is the density sampled in a (100) plane through the solid, which ranges from black (low density) to yellow (high density); with the positions of the nuclei denoted by white circles. Here the valence electrons occupy octahedral interstitial sites. (*B*) Same plot for cI16 Li solid at high density $\rho = 1.3$ g/cm^3. Here the electrons occupy positions within trapezoids of nuclei, and between neighboring atoms bridging the trapezoidal chains.

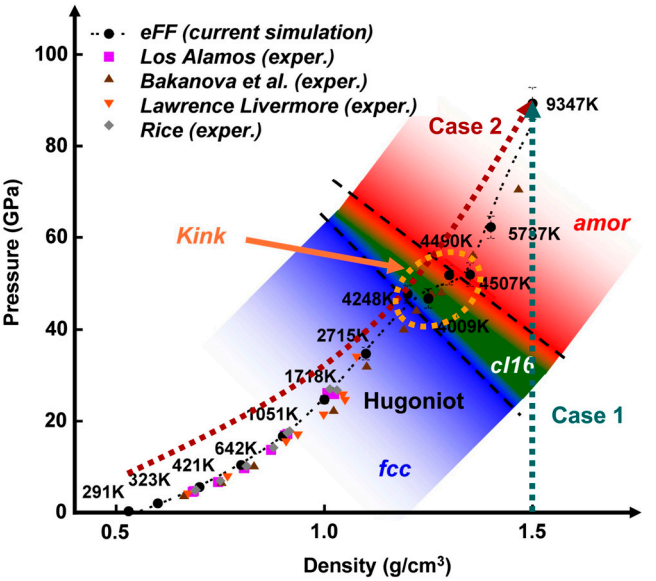

Fig. 2. Shock Hugoniot curve for solid Li computed from eFF dynamics (black circles and red dashed line) agrees well with experiment (violet squares from ref. 28, brown triangles from ref. 29, orange reverse triangles from ref. 30, and gray diamonds from ref. 31). The computed T at each ρ is shown with text on the plot. Both the eFF and experimental shock Hugoniot curves show a kink at 1.2–1.3 g/cm^3 and approximately 50 GPa. The eFF structural analyses show that this kink results from two closely spaced phase transitions: a solid-solid transition at 1.21 g/cm^3 and 47 GPa (close to the values of $\rho = 1.20$ g/cm^3 and $P = 40$ GPa calculated with eFF at 300 K in isothermal compression and the values of $P = 45$ GPa from experiment; Fig. S7); and a second, a cI16-to-amor phase transition at 1.33 g/cm^3 and 52 GPa. To access the high pressure and high temperature phase of amor, we further investigated two other thermodynamic paths: Case 1: Heating up the compressed system at $\rho = 1.5$ g/cm^3 a from 300 to 10,000 K, and, Case 2: Compressing the system from the ambient density of 0.53 g/cm^3 to 1.5 g/cm^3 under high temperature of 10,000 K. The results are analyzed in Fig. 4.

For $\rho \leq 1.2$ g/cm^3, the g(r) exhibits a clear fcc pattern with CN = 12. Near 1.3 g/cm^3, the g(r) pattern changes dramatically, while still showing long range order. This pattern matches that of the cI16 solid, leading to the same CN (10.9 at 4,009 K, compared to 11 for the ideal cI16 solid) although the peak positions are severely broadened due to the elevated T of the system (4,009 K).

Above 1.4 g/cm^3, the pattern of g(r) changes dramatically from that of cI16 phase. The long range order in g(r) disappears (the third peak of g(r) is nearly gone) and the CN drops to 9.48 at 1.4 g/cm^3 and 9.29 at 1.5 g/cm^3. This phase, which we denote as amor, represents a state of lithium whose structural and electronic properties have not been described previously.

To quantify the transition to the amor phase, we compare the ratio of peak height at the second minimum and peak height at the third maximum, which shows a large increase at 1.32 g/cm^3 (see Fig. S8*C*). We find that the combination of the fcc-to-cI16 transition plus the cI16-to-amor transition is responsible for the kink observed in both the experimental and eFF Hugoniot curves.

To further characterize the amor phase, we define a topological connectivity distribution function, P(n), where one by one we examine each bond pair (IJ) and ask how many other atoms, n, are bonded to both I and J. [The bond length is based on the distance to the first minimum in the g(r) after the first maximum.] This connectivity distribution function, P(n), quantifies how the connectivity is locally clustered among the nearest neighbors of a specific bond. For fcc crystal, $P_{fcc}(4) = 1$ whereas all other $P_{fcc}(n) = 0$; for cI16 crystal, $P_{cI16}(3) = 8/11$, $P_{cI16}(4) = 3/11$,

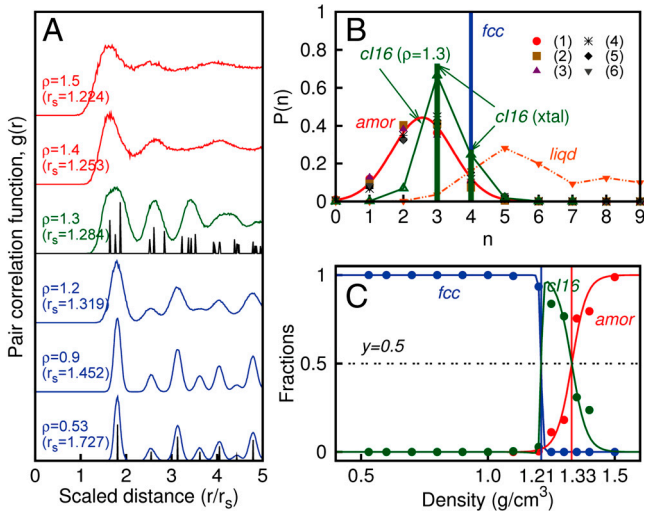

Fig. 3. (*A*) Nuclear-nuclear pair correlation function g(r). This shows a loss of order, with well-defined solid peaks vanishing as ρ increases from 1.2 g/cm^3 to 1.4 g/cm^3. For consistency, g(r) is plotted as a function of the scaled distance, r/r_s. (*B*) Comparison of the topological index P(n) (number of atoms bonded to both atoms of each bond) for the various phases from eFF trajectories. The blue and green lines indicate P(n) for fcc and cI16, respectively. For the amor phase, we examined six slightly different conditions (listed below) all of which exhibit a similar P(n) behavior. Indeed this composite P(n) function is well fitted by a Gaussian function G(n) centered at 2.6 with a width of 0.9. We interpret this to indicate that all these cases correspond to the same amor phase. In contrast the normal liqd phase of Li (orange line*) shows higher CN (16 vs. 9) and a much broader P(n) distribution. The six amor cases are: (*i*) $\{\rho,T\} = (1;$ the point on the Hugoniot curve$)\{1.5,9347\}$, (*ii*)$\{1.5,10580\}$, (*iii*)$\{1.5,19910\}$, (*iv*)$\{1.4,10050\}$, (*v*)$\{1.4,15260\}$, and (*vi*)$\{1.4,19720\}$. (*C*) Fractional compositions of the Li phases along the Hugoniot curve based on P(n). The f_{fcc} and f_{amor} fitted by a hyperbolic tangent function of the form $0.5[1-\tanh[a(x-x_c)]]$, where $\{a,x_c\} = \{134.83,1.21\}$ for fcc and $\{a,x_c\} = \{-17.00,1.33\}$ for amor. This leads to a fcc-to-cI16 transition at 1.21 g/cm^3 and the cI16-to-amor transition at 1.33 g/cm^3.

and $P_{cI16}(n) = 0$ otherwise. This connectivity distribution function is related to the Honeycutt–Anderson (HA) analysis (32).

To obtain P(n) of the amor phase, we analyzed six different simulation trajectories at $T = 10{,}000$–$20{,}000$ K and $\rho = 1.4$–1.5 g/cm^3 (one is from the 1.5 g/cm^3 case is on the Hugoniot curve). All lead to the same form for $P_{amor}(n)$ as shown in Fig. 3*B*, indicating that P(n) is a good order parameter for characterizing the amor phase. Interestingly, we find that $P_{amor}(n)$ is fitted well by a Gaussian distribution function ($R^2 = 0.98$); with mean value of $n = 2.6$ and a standard deviation is 0.9. Because P(n) for a random graph is a binomial distribution (whose large N limit is a Gaussian distribution; $N =$ number of samples), this implies that the amor phase has a nearly random clustering with an average of 2.6 neighbors per bond pair.

To describe the phase transition quantitatively, we write the P(n) of each system as a linear combination of $P_{fcc}(n)$, P_{cI16} (n), and P_{amor} (n):

$$P(n) = f_{fcc}P_{fcc}(n) + f_{cI16}P_{cI16}(n) + f_{amor}P_{amor}(n) + E, \qquad [1]$$

where f_{fcc}, f_{cI16}, and f_{amor} are the composition fractions of the fcc, cI16, and amor phases, respectively. We used a least squares procedure to fit P(n) subject to the constraints that all coefficients are nonnegative. The magnitude of the residual function E, when squared, never exceeded 0.05, validating our assumption that Eq. **1** holds.

*Liquid phase under low pressure is generated by the eFF simulation at 0.53 g/cm^3 and 9,388 K.

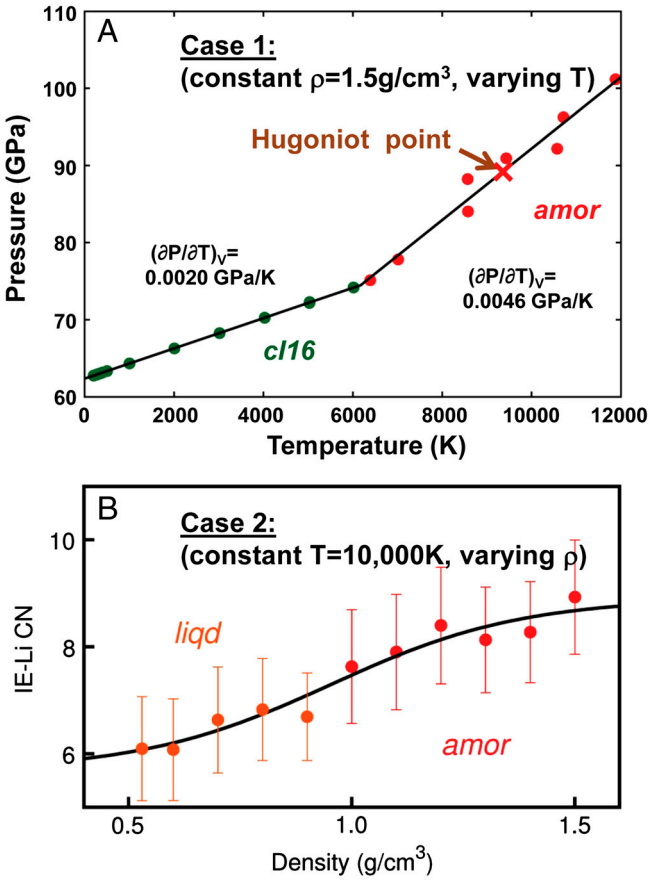

Fig. 4. (*A*) Change of pressure while heating up the system under high compression (Case 1 of Fig. 2). This shows that the slope of amor phase is 2.3 times larger than that of cI16 phase, indicating that the amor phase has a much larger entropy than the crystalline phase of cI16. (*B*) Change in the number of nuclei coordinated to each interstitial electron during the isothermal compression at 10,000 K (Case 2 of Fig. 2). Under low compression, valence electron of liqd phase is coordinated by approximately 6 Li^+ nuclei. Under high compression, the Li CN increases until approximately nine suggesting that the compression induces more significant IE–Li interactions while sacrificing the Li–Li interaction (resulting from inner-shell formation). This is very similar to the phase transition from fcc to cI16 (compare Li CN of fcc and cI16 are six and eight, respectively).

The coefficients obtained from this fit along the primary Hugoniot curve are shown in Fig. 3*C*. We find that along the Hugoniot, the system is 100% fcc solid for $\rho \leq 1.1$ g/cm^3, with f_{fcc} then dropping rapidly to 0 by 1.3 g/cm^3, with the transition at 1.21 g/cm^3. Simultaneous with this decrease of f_{fcc}, f_{cI16} dramatically increases attaining 84% cI16 character at 1.25 g/cm^3, along with 11% of the amor phase. Then, the cI16 phase disappears by $\rho = 1.5$ g/cm^3 with the second phase transition at 1.33 g/cm^3. We note that this transition at ρ of 1.33 g/cm^3 matches the transition density of $\rho = 1.32$ g/cm^3 deduced from the disappearance of the third peak in g(r) in Fig. 3*C*.

We also examined the mean squared displacement (MSD) to provide a measure of the diffusion rate. The MSD of the amor phase shows fluidity three times that of the solid cI16 (or fcc) phases (see Fig. S9).

Next we compare the amor phase with the liquid phase (liqd) found at high T but low P. Fig. 3*B* shows that the topological indices of Li–Li bonding, $P_{liqd}(n)$ vs. $P_{amor}(n)$, are quite distinct. Thus liqd has a P(n) of four to seven neighbors to each bond, and deviates significantly from the Gaussian distribution for amor as shown in Fig. 3*B*.

To further clarify the comparison of the amor phase to other phases, we investigated the equation of states for two cases.

1. Case 1: Constant $\rho = 1.5$ g/cm^3 with T increasing from 300 to 10,000 K (cI16-to-amor phase transition in Fig. 2), and
2. Case 2: Isothermal compression at $T = 10{,}000$ K from a density of 0.53 to 1.5 g/cc (liqd-to-amor phase transition; in Fig. 2).

Case 1 leads to the P vs. T at 1.5 g/cm^3 shown in Fig. 4*A*. Here $(\partial P/\partial T)_V = 0.0020$ GPa/K for cI16 whereas $(\partial P/\partial T)_V = 0.0046$ GPa/K for amor. From Maxwell's relations $(\partial P/\partial T)_V = (\partial S/\partial V)_T$, the entropy change per volume change at constant temperature. This indicates that the amor phase has 2.3 times larger entropy than the cI16 phase. This implies that the "increased T" at the shock wave front is more responsible than the "increased P" for the transition from the ordered crystalline phase (energetically favored phase) to the amor phase (entropically favored phase).

Then, we analyzed the change of g(r) during the isothermal compression at 10,000 K (Case 2; refer Fig. S10*A*). The CN of liqd phase at $\rho = 0.53$ g/cm^3 is nearly 16, much larger than the CN of amor phase, approximately nine. Until 1.0 g/cm^3, the compression increases the CN of Li monotonically, a pattern typical for fluids (33). At 1.0 g/cm^3, we observe that an inner-shell structure develops [appearing as a new second peak, which decreases the CN (see Fig. S10*B*)] by changing the bond distance The physical origin of the formation of the inner-shell structure is suggested from the IE-Li$^+$ coordination number in Fig. 4*B*. At 0.53 g/cm^3, the IE of liqd phase shows that each electron is surrounded by approximately six Li$^+$ ions (as in the fcc phase), but the compression increases the number of Li$^+$ ions coordinating an IE until approximately nine at 1.5 g/cm^3 (versus the lower IE-Li$^+$ coordinations of six and eight for fcc solids and cI16 solids, respectively). Fitting to a hyperbolic tangent function leads a transition point at 0.95 g/cm^3, at which the inner shell forms. This indicates that the driving force of liqd-to-amor phase transition is rooted on the same physical origin that governs the fcc-to-cI16 phase transition; extremely high pressure induces more IE–Li interactions while sacrificing Li–Li interactions, leading to an increasing IE–Li CN and decreasing Li–Li CN. Based on the Li CN of IE, we conclude that the fluidic phases under high T, liqd and amor, have local IE–Li interactions similar to that of the solid phases under low T, fcc and cI16, respectively.

We expect that the amor phase will have a lower electrical conductivity than the liqd phase because of increased interaction between valence electrons and nuclei, just as in the comparison of cI16 and fcc cases. This lower fluidity of valence electrons (see Fig. S11) is related to the actual diffusion of orbitals. Experiments on the changes in the electrical conductivity along the Hugoniot might provide an experimental measure for observing the liqd-to-amor phase transition.

Summarizing, we find that the simple eFF method (using the same functional form, parameters, and potentials as for the applications to the hydrogen Hugoniot and the Auger dynamics of diamondoids) captures accurately complex phase transitions exhibited by Li up to 20,000 K and 100 GPa, indicating that eFF can describe systems with both localized core elections and diffuse metallic bonding electrons. The eFF leads to an excellent description of the fcc-to-cI16 transition at 40 GPa and 300 K, as well as the more complex series of phase transitions that occurs during dynamic shock compression of Li: fcc-to-cI16 at 1.21 g/cm^3 and cI16-to-amor transition at 1.33 g/cm^3. Moreover eFF provides an atomistic interpretation of the shock experiments explaining the kink in the Hugoniot curve at 1.2–1.3 g/cm^3 as a consequence of the consecutive phase transformations to cI16 and then amor. Our simulations indicate that the amor phase for Li generated by shock compression has a very distinct local topology compared to that of a liqd phase at low P, characterized by a random clustering of atoms about each bond with an average packing (2.5 atom neighbors per bond) much less dense than liqd (five atom neighbors per bond) and a suppressed fluidity. The high compression maximizes valence electron–nucleus interactions while sacrificing nuclei–nuclei interaction just as in the formation of cI16 phase, but at much higher T, inducing a phase transition from a crystalline cI16 phase to the entropically favored phase of amor phase.

Notably, eFF captures the subtle shift of core-valence interactions responsible for the coupled electronic-structural fcc to cI16 transition at 300 K, while also capturing the extended dynamics of nuclear motions and electronic excitations that govern the relative stability of many different phases at high P and T. This suggests that eFF will be useful for describing the structural, energetic, and electronic properties of warm, dense matter containing complex combinations of covalent, ionic, and metallic bonding.

Methods

The eFF Dynamics. We performed the eFF dynamics for total simulation times of 1–2 ps with 1– 2 ps of preequilibration and a time integration step of dt = 5 attoseconds. With eFF the time-dependent Schrödinger equation uses an empirical exchange term with three universal parameters that are exactly the same as in previous publications (6–8). Individual trajectories were integrated in the microcanonical ensemble. We equilibrated the Li system at each temperature by starting with an energy-minimized geometry, giving the nuclei a Maxwell–Boltzmann distribution of initial velocities. By varying the initial velocity distributions temperature, we obtained a correct final temperature with energy properly partitioned between all degrees of freedom. Either periodic fcc ($3\times3\times3$ supercell, 108 atoms) or cI16 ($2\times2\times2$ supercell, 128 atoms) lattices were employed as an initial structure for the simulations.

Theoretical Shock Hugoniot Curve. For each density, we started the simulation with two different crystal structures of fcc and cI16. Then, we determined the P, T, and E conditions satisfying Rankine–Hugoniot conditions with both initial structures. Between two sets of P, T, and E determined from two independent initial structures, we chose the set having the lower internal energy E. This procedure yields initial structures of (*i*) fcc structures, when $0.53 \le \rho < 1.2$ g/cm^3, and (*ii*) cI16 structures, otherwise. These initial conditions are identical to the conditions having the lower internal energies during the 300 K isothermal compression (see Fig. S7).

ACKNOWLEDGMENTS. This work was supported by Defense Advanced Research Planning Agency–Office of Naval Research (PROM), the US Department of Energy (Predictive Science Academic Alliance Program), and WCU [through the National Research Foundation of Korea funded by the Ministry of Education, Science, and Technology (R31-2008-000-10055-0)].

1. Hawreliak J, et al. (2007) Modeling planetary interiors in laser based experiments using shockless compression. *Astrophys Space Sci* 307:285–289.
2. Jeanloz R, et al. (2007) Achieving high-density states through shock-wave loading of precompressed samples. *Proc Natl Acad Sci USA* 104:9172–9177.
3. Nellis WJ, et al. (1983) Equation-of-state data for molecular-hydrogen and deuterium at shock pressures in the range 2–76 GPa (20–760 KBar). *J Chem Phys* 79:1480–1486.
4. Knudson MD, Hanson DL, Bailey JE, Hall CA, Asay JR (2003) Use of a wave reverberation technique to infer the density compression of shocked liquid deuterium to 75 GPa. *Phys Rev Lett* 90:035505.
5. Boriskov GV, et al. (2005) Shock compression of liquid deuterium up to 109 GPa. *Phys Rev B* 71:092104.
6. Su JT, Goddard WA (2009) The dynamics of highly excited electronic systems: Applications of the electron force field. *J Chem Phys* 131:244501.
7. Su JT, Goddard WA (2007) Excited electron dynamics modeling of warm dense matter. *Phys Rev Lett* 99:185003.
8. Su JT, Goddard WA (2009) Mechanisms of Auger-induced chemistry derived from wave packet dynamics. *Proc Natl Acad Sci USA* 106:1001–1005.
9. Hanfland M, Loa I, Syassen K, Schwarz U, Takemura K (1999) Equation of state of lithium to 21 GPa. *Solid State Commun* 112:123–127.
10. Hanfland M, Syassen K, Christensen NE, Novikov DL (2000) New high-pressure phases of lithium. *Nature* 408:174–178.
11. Kietzmann A, Redmer R, Desjarlais MP, Mattsson TR (2008) Complex behavior of fluid lithium under extreme conditions. *Phys Rev Lett* 101:070401.
12. Fortov VE, et al. (2002) Lithium at high dynamic pressure. *J Phys-Condes Matter* 14:10809–10816.
13. Bastea M, Bastea S (2002) Electrical conductivity of lithium at megabar pressures. *Phys Rev B* 65:193104.

14. Gregoryanz E, et al. (2008) Structural diversity of sodium. *Science* 320: 1054–1057.
15. Maksimov EG, Magnitskaya MV, Fortov VE (2005) Non-simple behavior of simple metals at high pressure. *Phys-Usp+* 48:761–780.
16. Mazevet S, Zerah G (2008) Ab initio simulations of the K-edge shift along the aluminum Hugoniot. *Phys Rev Lett* 101:155001.
17. Pickard CJ, Needs RJ (2010) Aluminum at terapascal pressures. *Nat Mater* 9:624–627.
18. Olinger B, Shaner JW (1983) Lithium, compression and high-pressure structure. *Science* 219:1071–1072.
19. McAdon MH, Goddard WA (1985) New concepts of metallic bonding based on valence-bond ideas. *Phys Rev Lett* 55:2563–2566.
20. Neaton JB, Ashcroft NW (1999) Pairing in dense lithium. *Nature* 400:141–144.
21. Christensen NE, Novikov DL (2001) Predicted superconductive properties of lithium under pressure. *Phys Rev Lett* 86:1861–1864.
22. Christensen NE, Novikov DL (2002) Calculated properties of high-pressure phases of "simple metals". *J Phys-Condes Matter* 14:10879–10883.
23. Rodriguez-Prieto A, Bergara A, Silkin VM, Echenique PM (2006) Complexity and Fermi surface deformation in compressed lithium. *Phys Rev B* 74:172104.
24. Silkin VM, Rodriguez-Prieto A, Bergara A, Chulkov EV, Echenique PM (2007) Strong variation of dielectric response and optical properties of lithium under pressure. *Phys Rev B* 75:172102.
25. Tamblyn I, Raty JY, Bonev SA (2008) Tetrahedral clustering in molten lithium under pressure. *Phys Rev Lett* 101:075703.
26. Li M, Goddard WA (1989) Interstitial-electron model for lattice-dynamics in fcc metals. *Phys Rev B* 40:12155–12163.
27. Erpenbeck JJ (1992) Molecular-dynamics of detonation 1. Equation of state and Hugoniot curve for a simple reactive fluid. *Phys Rev A* 46:6406–6416.
28. Marsh SP (1980) *LASL Shock Hugoniot Data* (University of California Press, Berkeley).
29. Bakanova AA, Dudolado IP, Trunin RF (1965) Compression of alkali metals by strong shock waves. *Sov Phys-Sol State* 7:1307–1313.
30. van Thiel M, ed. (1977) *Compendium of Shock Wave Data* p 323 Lawrence Livermore Laboratory Report UCRL-50108, Livermore.
31. Rice MH (1965) Pressure-volume relations for the alkali metals from shock-wave measurements. *J Phys Chem Solids* 26:483–492.
32. Honeycutt JD, Andersen HC (1987) Molecular-dynamics study of melting and freezing of small Lennard-Jones clusters. *J Phys Chem* 91:4950–4963.
33. Hu JW, Duan ZH (2005) Theoretical prediction of the coordination number, local composition, and pressure-volume-temperature properties of square-well and square-shoulder fluids. *J Chem Phys* 123:244505.